SSRG International Journal of Electronics and Communication Engineering
ISSN: 2348-8549/ https://doi.org/10.14445/23488549/IJECE-V13I11P102

Volume 13 Issue 11, 25-39, November 2026
© 2026 Seventh Sense Research Group®

Original Article

Data Association and Track Classification using Random Forest and Spatiotemporal Filtering for Millimeter-Wave Radar

Venkatesha K[1], Upasna Singh[2], Vengadarajan A[3]

[1,2]*CSE, Defence Institute of Advanced Technology, Pune, India.*
[3]*Formerly with LRDE, DRDO, Bengaluru, India.*

[1]*Corresponding Author: venkatesha_pee20@diat.ac.in*

Received: 21 September 2026 Revised: 16 October 2026 Accepted: 23 October 2026 Published: 27 November 2026

Abstract *- The Advanced Driver Assistance System (ADAS) is growing rapidly worldwide. A core requirement for any ADAS is the ability to accurately track both on-the-road vehicles and pedestrians. However, tracking these targets using radar mounted on a moving vehicle, or ego vehicle, presents unique challenges. A key challenge is distinguishing stationary objects, such as roadside poles and trees, from approaching vehicles. Hence, it is essential to distinguish between them so that the ADAS can take appropriate safety measures. This article introduces an innovative method for associating radar detections using Random Forest (RF) to form meaningful clusters, along with a spatiotemporal filtering approach to differentiate stationary objects from inbound targets. By employing a multivariate RF that incorporates range, Doppler, and Angle of Arrival (AoA) as key variables, the algorithm effectively clusters the radar detections. The Kalman filter then tracks the targets. The spatiotemporal filter further classifies them as stationary or non-stationary. The algorithm has been rigorously validated in real-world scenarios, with a millimeter-Wave (mmWave) radar mounted on a vehicle and driven on the road to capture data on both stationary and moving targets. Multiple experiments were conducted to ensure the methodology's robustness, yielding commendable results with an accuracy rate of approximately 93%.*

Keywords *- ADAS, Kalman filter, Millimeter Wave Radar, Random Forest.*

1. Introduction

Autonomous vehicles are becoming a reality due to significant advancements in driver assistance systems, enhancing the safety of both passengers and other road users [1]. Radars are integral to ADAS systems. These radars use Frequency-Modulated Continuous Wave (FMCW) technology combined with the Multiple-Input Multiple-Output (MIMO) concept and operate in the millimeter-Wave (mmWave) frequency range [2]. Because of their compact design and ability to operate effectively in various weather conditions, mmWave radars have become essential in ADAS [3]. Accurate target tracking is crucial, as timely detection is vital. Therefore, robust radar signal processing is essential. Authors in [4] provide an overview of signal-processing algorithms relevant to ADAS applications. An overview of signal modeling and the extraction of range, Doppler, and Angle of Arrival (AoA) can be found in [5]. The challenges in signal processing pertaining to automotive radars are discussed in [6]. Multitarget tracking is essential for autonomous radars. Before target tracking, radar detections must be grouped into appropriate clusters based on range, Doppler, AoA, and other parameters. The new detections must be associated with the correct clusters. One widely used data-association technique is Joint Probabilistic Data Association (JPDA) [7]. The limitation is resolving close-proximity targets. To improve performance, the authors in [8] proposed the Cauchy-Schwarz set JPDA. In this method, the set is optimized using a posterior Gaussian mixture density using iterative component-based optimization. The authors concluded that the proposed method offers a good trade-off between computational speed and the required target-tracking accuracy. Authors in [9] proposed a technique that transforms detections in the Range-Doppler and AOA domains to the Range-Angle domain using a weighted Density-Based Spatial Clustering of Applications with Noise (DBSCAN) algorithm. By estimating the centroid of the valid cluster points, the authors proposed accurate target tracking for autonomous radars. Associating detections in a dense target environment is challenging. Authors in [10] proposed PointNet++-based radial-velocity sampling and hyperparameter optimization for detection in mmWave radar using point cloud data. Building on DBSCAN-based detection clustering, the authors in [11] proposed modifying the DBSCAN epsilon parameter to adjust the DBSCAN cluster shape for improved performance. In

This is an open access article under the CC BY-NC-ND license (http://creativecommons.org/licenses/by-nc-nd/4.0/)

contrast, for automotive radar detection clustering, the authors in [12] proposed Topographical Density Mapping (TDM), which achieves performance similar to DBSCAN-based methods while handling complex target scenarios. To improve DBSCAN-based clustering for autonomous vehicle applications, the authors in [13] proposed an enhanced multiple DBSCAN method that adjusts parameters based on distance to reduce cluster size, achieving over 90% accuracy. The authors indicate that using a multiple DBSCAN approach in conjunction with Non-Maximum Suppression (NMS) can effectively address missing detections. Similarly, authors in [14] used multi-dimensional DBSCAN to associate detections in mmWave radars. Clustering is performed in two stages: first, velocity-based, then in the spatial domain.

In a multilayered approach, authors in [15] proposed Layered Doppler Position Clustering (LDPC), which uses Doppler and position data to cluster point cloud data. In this method, the authors defined three layers. The first layer separates static and dynamic detections, the second performs pre-clustering using one-dimensional hierarchical clustering, and the last layer performs clustering using DBSCAN and positional data.

Further, to address false and erroneous detections due to multipath, etc., the authors in [16] proposed the PointNet++ network architecture for clustering. The architecture combines the three feature branches and applies self-attention for discrimination. The proposed algorithm uses DBSCAN in the first stage to cluster based on radial velocity and Radar Cross Section (RCS), then uses the extracted features for more detailed clustering.

In a different approach, the authors in [17] proposed a Piece-Meal-based solution. In the proposed article, data points that are close in Euclidean distance and similar in cosine similarity are kept in the same cluster. The threshold is adjusted adaptively to address challenges related to prior knowledge about the dataset. In a different approach, authors in [18] proposed Generalized Label Multi Bernoulli δ−(GLMB) for filtering and DBSCAN for clustering. With δ−GLMB filtering, the authors proposed using DBSCAN to determine the target cluster in real time, then estimate the target's associated collaborative noise to correct the predicted target position. The authors reported that the proposed technique is very effective when clusters split, reorganize, and merge. In another approach, authors in [19] proposed an unsupervised DBSCAN clustering method using automatic fuzzy clustering.

In a different approach, the authors propose multi-sensor data fusion for data association and tracking. In [20], the authors proposed gathering spatial information from multiple sensors. By combining the cost, volume and regression, they predict range information. In [21], the authors propose radar-camera data fusion. They proposed D-FusionNet. The model combines data-level fusion with incremental learning using a Domain-Incremental Model (Domain-IL). The authors reported that this method significantly improved ADAS sensor performance under adverse weather conditions. The authors in [22] proposed a technique that fuses depth information from radar and cross-range information from camera data and uses a tri-Kalman filter for tracking.

Authors in [23] provided an overview of recent advancements and challenges in target tracking with mmWave radars mounted on a moving vehicle. Doppler ambiguity is common in target tracking with mmWave radars. Authors in [24] proposed a MIMO- and time-division multiplexing-based solution that accurately estimates the AoA of the target echo signal and resolves velocity ambiguity. In [25], the authors provided insight into practical track management.

A common problem in ego-vehicle tracking is the intruder. They pose a real challenge for ADAS. One such solution can be found in [26]. Here, the authors proposed a solution that combines mmWave radar and a camera and uses DBSCAN, Global Nearest Neighbor (GNN), and an Extended Kalman Filter for data association and tracking. In another approach, the authors in [27] proposed delayed windowing before using the data for DBSCAN clustering.

1.1. Novelty of the Proposed Algorithm

Unlike the literature mentioned above, the proposed method is unique. The proposed method is for mmWave radar on the move. This differs significantly from static radars. The mobile radar tracks consist of returns from moving targets and static targets.

They must be distinguished. One approach is to subtract the measured speed from the ego-vehicle speed. This requires an additional interface that connects the ego-vehicle speedometer to the radar to record the ego-vehicle speed. However, the proposed method requires no additional interface to discern the stationary clutter from incoming targets.

The proposed algorithm introduces an innovative approach by leveraging spatial and temporal variations in Doppler, range, and Angle of Arrival (AoA) for target detection and tracking. It consists of two distinct phases. In the initial phase, the algorithm associates new detections with relevant clusters using Random Forest.

This data association process uses range, Doppler, and AoA as key discriminators. The second phase performs spatio-temporal filtering, classifying tracks as incoming targets, stationary clutter, ground reflections, or false alarms. For clarity, Figure 1 presents a range-versus-time plot showing false alarms, ground clutter, stationary targets, and the incoming vehicle.

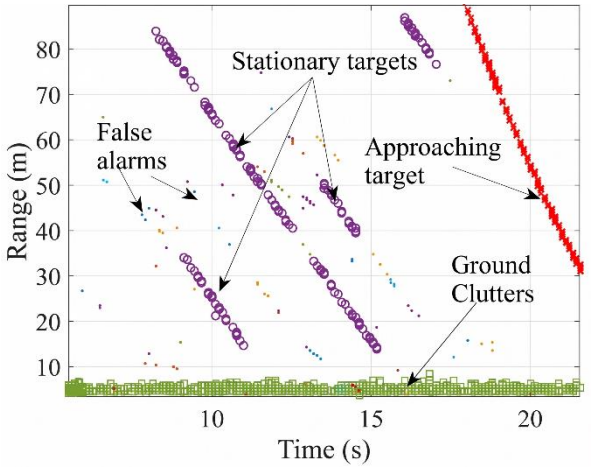

Fig. 1 Data association, tracking and classification

1.2. Key Contributions

The following are the key contributions of the research work:

- *Generation of a comprehensive dataset*: A number of experiments were conducted using an mmWave radar mounted on a car and driven on the road. The radar targets were both incoming and stationary. The collected real dataset was used to evaluate the proposed algorithm.
- *Random Forest dataset:* The training dataset for RF was created using a mathematical model based on proximity limits in the target range, Doppler, and AoA.
- *Target Discrimination Mode and tracking*: The proposed model uses a trained RF to discriminate the detections into clusters based on range, Doppler, and AoA. After data association, the Kalman filter tracks targets.
- *Spatio-temporal Filtering*: The proposed Spatio-temporal filter discerns the radar tracks into four classes: a: Incoming target, b: Stationary Clutter, c: Ground reflection clutter, d: False alarms.
- *Performance evaluation*: The performance of the proposed method was evaluated with a real-world dataset obtained through multiple experiments covering multiple scenarios.

The paper is organized as follows: Section 2: Problem formulation, Section 3: Proposed method, Section 4: Experiments and results, and Section 5: Conclusion.

2. Problem Formulation

2.1. Overview of the Conducted Experiments

Several experiments were conducted using an FMCW mmWave radar mounted on a car and driven on the road. The experimental platform comprised a mmWave radar (Texas Instruments (TI) AWR1843 BOOST), interfaced with a data acquisition card (TI DCA1000). The data acquisition card recorded the raw data during the experiment. The radar and data acquisition card were mounted on a car bonnet. Figure 2 shows the radar setup. The cards draw power from the car battery.

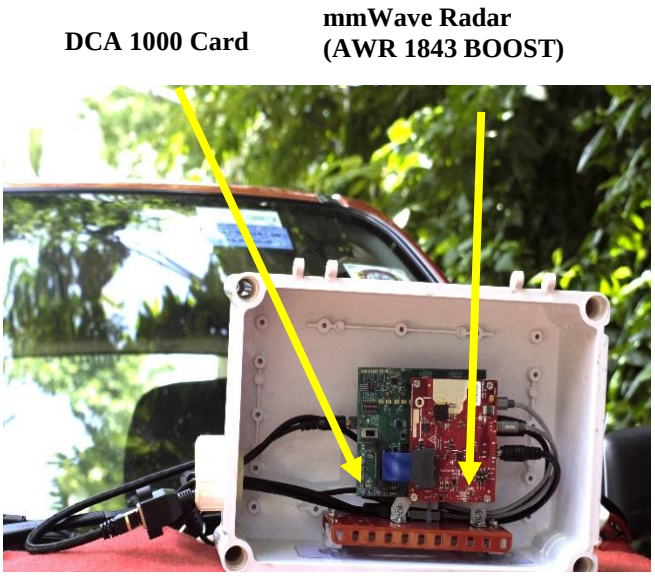

Fig. 2 mmWave radar mounted on a car

While moving, the radar captures raw data. The raw data comprises In-Phase and Quadrature (I/Q) components. The radar was configured to use an up-chirp waveform. The radar has $\mathcal{M}(\mathcal{M}=4)$ receive channels, and records digitized received data from all four channels after Analog-to-Digital Conversion (ADC) processing.

The experiments comprised multiple frames, each containing $\mathcal{L}$ $(\mathcal{L}=128)$ chirps, and each chirp containing $\mathcal{N}(\mathcal{N}=256)$ ADC samples. Thus, the total dataset in any frame can be visualized as a cuboid of dimension $\mathcal{N}\times\mathcal{L}\times\mathcal{M}$. In this case, the data cuboid is 256 × 128 × 4. The experiments comprised both stationary and incoming targets.

2.2. Receive Chain Signal Modeling

The mmWave radar used in this study is based on a monolithic construction, with three transmit and four receive antennas, and δ_{ele} is the spacing between two antenna elements. Here λ is the wavelength of the transmitted/received signal. Figure 3 illustrates the complete receive-chain processing.

Let, f_s denote the start and f_e the end frequency of the chirp, respectively. The bandwidth is expressed as $B=(f_e-f_s)$. Let T_c denote the chirp duration. The slope of the chirp ζ is given by $\zeta=B/T_c$. Further, let T_s be the ADC sampling time; then the sampling frequency is $F_S=1/T_s$. Assuming a target at range r_t from the radar, τ denotes the echo turnaround time.

The beat frequency, which is the difference between the transmitted frequency f_{tx} and the received target echo frequency f_{rx}, is given by $f_b=(f_{tx}-f_{rx})$ and, further, it can be represented by $f_b=\zeta\tau=2\zeta r_t/c$, where c is the speed of light in vacuum. Let $\omega_b=2\pi f_b/F_S$.

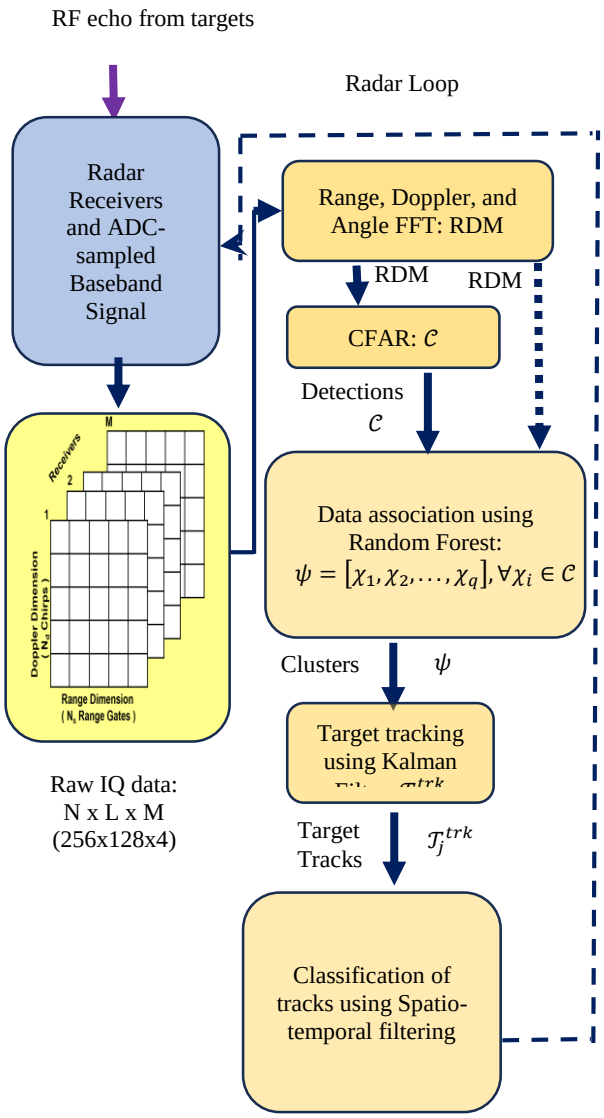

Fig. 3 Radar receive chain processing

Let $s_b[n]$ represent the discrete-time complex baseband signal at any receiver for any arbitrary chirp and is given by Equation (1) [5].

$$\phi_b \approx 2\pi f_c \tau, = 4\pi r_t/\lambda,$$
$$s_b[n] = Ae^{j\phi_b} e^{jn\omega_b},$$

where

A is the amplitude of the signal,

ϕ_b is the phase component of the baseband signal. (1)

2.3. Target Range Estimation

Further, the target range from the radar r_t is obtained by performing the Discrete Fourier Transform (DFT) on $s_b(n)$ as given by Equation (2), Where $S_B(k)$ is the range-DFT output of the signal $s_b(n)$. Detailed derivations are provided in [5].

$$S_B[k] = \mathcal{F}(s_b(n)),$$
$$= S_B(w_b)|w_b = 2\pi k/N_s$$
$$0 \le k \le (N_s - 1),$$

n is the current time index,

k is the current frequency index. (2)

Referring to the above Equation (2), the index k in $S_B[k]$ corresponds to frequency $f_k = kF_s/N_s$ and using the range relationship equation, the index of $S_B[k]$ can be converted to a range $r_k = f_k(c/2\zeta)$, [5]. The index cell is also referred to as the kth range cell or range gate.

2.4. Target Doppler Estimation

As discussed earlier, the radar transmits equally spaced $\mathcal{L}$ chirps with the chirp time of T_c in a frame. Let $s_d[k] = [S_b[k,1], S_b[k,2], \ldots S_b[k,L]$ be the $\mathcal{L}$ number-sampled range-DFT output of the kth range cell of all $\mathcal{L}$ chirps. Performing DFT on $s_d[k,l]$ provides Doppler-DFT $S_{RD}[k,p]$ as defined in Equation (3) [5].

$$S_{RD}[k,p] = \mathcal{F}(s_d(k))$$
$$= S_{RD}(k,\omega_d)|\omega_d = 2\pi p/\mathcal{L},$$
$$\forall\ 0 \le k \le N_s, 0 \le p \le \mathcal{L}$$

k is range cell index,

p is the Doppler Cell index. (3)

The term S_{RD} is a two-dimensional matrix of size $N_S \times \mathcal{L}$. Define the term Range Doppler Map (RDM) as $RDM = S_{RD}[k,p] \mid 0 \le k \le N_S,\ 0 \le p \le \mathcal{L}$.

The columns of RDM indicate range bins, and the rows indicate Doppler bins. The target velocity is derived from $v_t = \omega_d \frac{\lambda}{4\pi T_c}$. The RDM is used for the target detection process using the Constant-False-Alarm Rate (CFAR) algorithm.

2.5. AoA Estimation

The mmWave radar used here consists of $\mathcal{M}$ receivers, with the antenna element spacing of δ_{ele}. The delay in the arrival signal at two adjacent antenna elements is $\Delta_t = \delta_{ele} sin(\theta)/c$, where θ is AoA, and c is the speed of light. Unlike in previous cases, the Angle-DFT is performed only for valid detections after detection processing.

This avoids unnecessary AOA calculations over the entire RDM. Let the target detection set for the current RDM be denoted by $\mathcal{D}^{rdm}$.

Assume that there is a detection at m^{th} range cell and k^{th} Doppler cell, i.e., a detection at $RDM(k,p)$ after CFAR processing. Let $S_{RD}^{(m)}[k,p]$ denote the Doppler-DFT for receive channel m. The computation of the Angle-DFT is given in Equation (4) [5].

$$S_{ang}[k,p,m] = \mathcal{F}\left(S_{RD}^{(M)}[k,p]\right) = S_{ang}(k,p,w_a),$$

Where

$$S_{RD}^{(M)}[k,p] = \left[S_{RD}^{(1)}[k,p], S_{RD}^{(2)}[k,p], \ldots, S_{RD}^{(m)}[k,p]\right], \quad 1 \le m \le \mathcal{M},$$

Where $w_a = 2\pi m/\mathcal{M}$. (4)

The peak of the tensor $S_{ang}(k,p,w_a)$ indicates the AoA. Let the peak of the `tensor. $S_{ang}(k,p,w_a)$ indexed by m_a. The corresponding angle in radians θ_a can be computed by

$$\theta_a = sin^{-1}\left(m_a \frac{\lambda}{\mathcal{M}\delta_{ele}}\right), \quad -\mathcal{M}/2 \le m_a \le \mathcal{M}/2.$$

2.6. Target Detection Process

After computing the RDM, the detection process is performed. The target detection is performed using CFAR techniques. In this case, 2-Dimensional CFAR is performed. Common CFAR algorithms include Cell-Average CFAR (CA-CFAR), Greatest-of CFAR (GO-CFAR), Smallest-of CFAR, and Ordered Statistics CFAR (OS-CFAR) [28]. In this study, the OS-CFAR is used for detection processing.

The output of the CFAR process is a two-dimensional binary detection matrix represented as $\mathcal{C}$. The matrix has the same dimensions as the RDM, i.e., $N_S \times \mathcal{L}$, indicating the range and Doppler cell indices representing the detections. A true ('1') in a cell indicates a detection, and a false ('0') indicates no detection.

Angle estimation is performed using Equation (4) only for the valid detections in $\mathcal{C}$. The corresponding angles for the valid detections are stored in a matrix $\mathcal{A}$ having dimension. $N_S \times \mathcal{L}$, the same dimension as $\mathcal{C}$.

2.7. Data Association

In any experiment, the FMCW radar continuously transmits and receives simultaneously, and the data cuboid of dimension $\mathcal{N} \times \mathcal{L} \times \mathcal{M}$ is formed. For each cuboid, one RDM and one detection matrix $\mathcal{C}$ are obtained.

Based on the detections in $\mathcal{C}$, the range is computed using Equation (2), the Doppler from (3), and the angle from (4). For every detection, a 3D tensor is formed, denoted by χ_i, containing: target range from radar, target Doppler, and target AoA, represented as $\chi_i = (r_i, d_i, a_i)$. The array of tensors denoted by ψ is represented in Equation (5), assuming. q number of detections in the current detection matrix $\mathcal{C}$.

$$\psi = [\chi_1, \chi_2, \ldots, \chi_q], \forall \chi_i \in \mathcal{C}. \quad (5)$$

The proposed RF-based algorithm uses ψ for data association. The output of this stage is a set of spatio-temporal tensors denoted as ρ_j, containing closely associated tensors based on range, Doppler, and angle in the spatial domain and time in the temporal domain. The ρ_j corresponds to a jth track.

2.8. Tracking and Spatio-Temporal Filtering

Target tracking is performed using the Kalman Filter (KF). The updated ρ_j are used by KF for tracking. The tracks are classified based on both the target's spatial and temporal characteristics. The following section explains the proposed RF algorithm and spatio-temporal filtering.

3. Proposed Algorithm

The algorithm consists of three stages. In the first stage, the trained RF performs data association. In the second stage, tracking is performed using KF on the dataset. ρ_j. The third stage classifies the tracks using spatio-temporal filtering.

3.1. Random Forest-based Data Association

In this article, a Trivariate Random Forest (TRF) associates new detections with the tracks. The RF uses range, Doppler, and AoA as variables.

The association is based on the absolute difference between the tensors of new detections, namely χd and the latest tensor of active tracks, χ_i^t.

The difference tensor is denoted as χ_i^δ, and it is used as input to the TRF. Computation of χ_i^δ is provided in Equation (6). The output of the TRF is the degree of neighborhood, a scalar denoted by Γ_i having values between *0* and *1*.

A value of *0* indicates the lowest association, or neighborhood degree, whereas a value of 1 indicates the highest association, or neighborhood degree. The Γ_i is computed using TRF for every active track.

In addition, the gating test is performed; the Γ_i is compared with a threshold T^{th}. If it crosses the threshold, the new detection is considered for association with the track.

If more than one track passes the gating test, the new detection is associated with the track with the highest Γ_i. If the gating test fails for all active tracks, the new detection is declared a false alarm. Figure 4 depicts the TRF-based association algorithm.

Tensor of a new detection

$$\chi d = (r_d, d_d, a_d).$$

Tensor of the latest element of an active track: *i*

$$\chi_i^t = (r_i, d_i, a_i).$$

Delta difference

$$r_{\delta_i} = |r_d - r_i|,$$
$$d_{\delta_i} = |d_d - r_i|,$$
$$a_{\delta_i} = |a_d - r_i|,$$
$$\chi_i^\delta = \left(r_{\delta_i}, d_{\delta_i}, a_{\delta_i}\right). \quad (6)$$

After data association, the Kalman filter tracks the target.

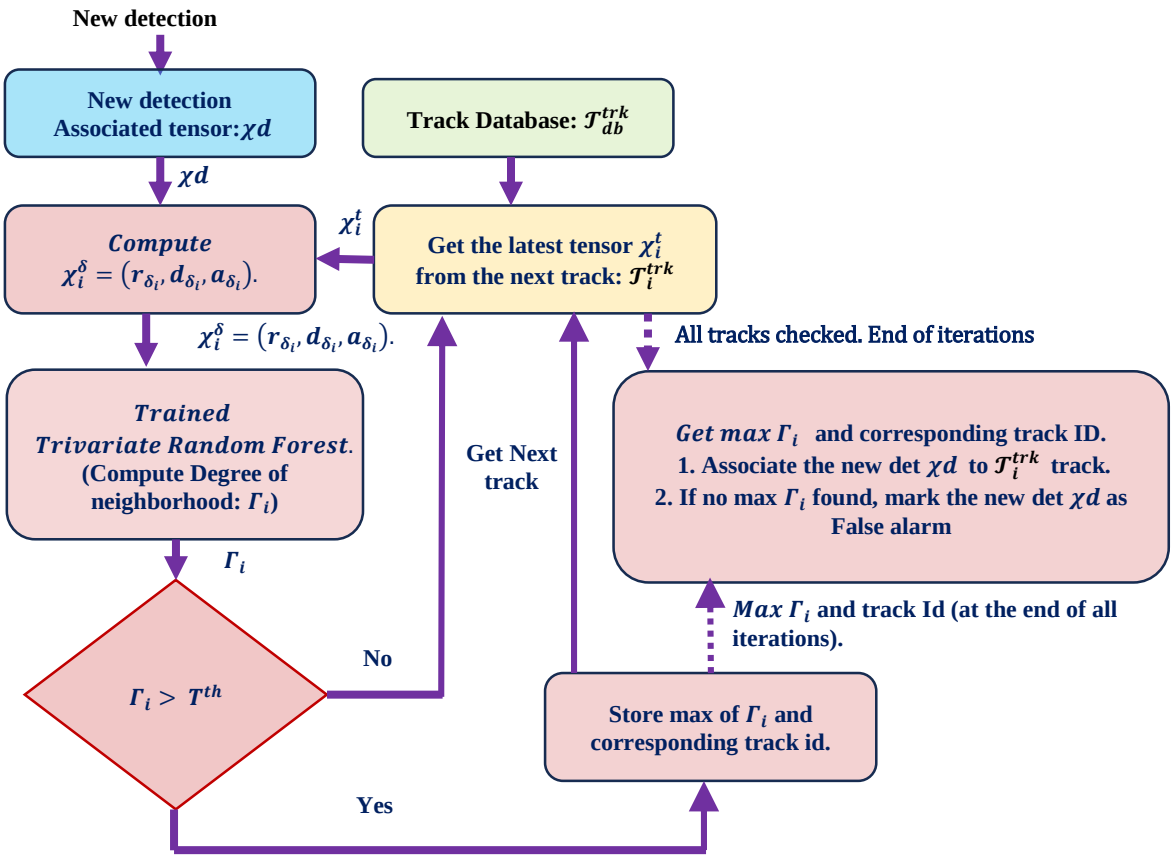

Fig. 4 TRF algorithm

3.2. Training TRF

The TRF is trained using synthesized data. The input dataset consists of an array of tensors denoted by χ^{trn}.

Let the array contain N_t tensors for training. The array contains individual training tensors as represented in Equation (7). The TRF regressor was trained with 100 trees.

The tensor elements are Gaussian random numbers in the interval from 0 to half the variable's maximum value.

For example, if the radar's maximum instrumented detection range is r_{max}, then the tensor element values for range are generated between *0* and $r_{max}/2$.

TRF input tensor generation

$$\chi^{Trn} = [\chi_1^{tr}, \chi_2^{tr}, \ldots, \chi_{N_t}^{tr}],$$
$$\chi_i^{tr} = (r_i^{tr}, d_i^{tr}, a_i^{tr}),$$
$$r^{tr} \simeq \mathcal{N}\,|(0: r_{max}/2),$$
$$d^{tr} \simeq \mathcal{N}\,|(0: d_{max}/2),$$
$$a^{tr} \simeq \mathcal{N}\,|(0: a_{max}/2),$$

where r_{max}, d_{max} and a_{max} are the maximum values for range, Doppler and AoA, respectively. (7)

The TRF output is a scalar. The expected output is computed from the input tensors. χ^{Trn}. The output of the TRF is denoted by Γ_i. Equation (8) gives the output computation.

The input tensor $\chi_i^{tr} = (r_i^{tr}, d_i^{tr}, a_i^{tr})$.

The function for input tensor normalization.

$$r_i^{TR} = 1 - \frac{|r_i^{tr}|}{r_{max}},$$
$$d_i^{TR} = 1 - \frac{|d_i^{tr}|}{d_{max}},$$
$$a_i^{TR} = 1 - \frac{|a_i^{tr}|}{a_{max}}.$$

The Weight vector: $W = (w_r, w_d, w_a)$.

Computation of the output of TRZ: Γ_i

$$\Gamma_i = r_i^{TR}\, w_r + d_i^{TR}\, w_d + a_i^{TR}\, w_a. \quad (8)$$

Where r_{max}, d_{max} and a_{max} are the maximum values for range, Doppler, and AoA, respectively. The RF is trained with χ^{Trn} as input parameters, and the expected output is Γ_i. Figure 5 shows the pruned Random Forest tree generated after training.

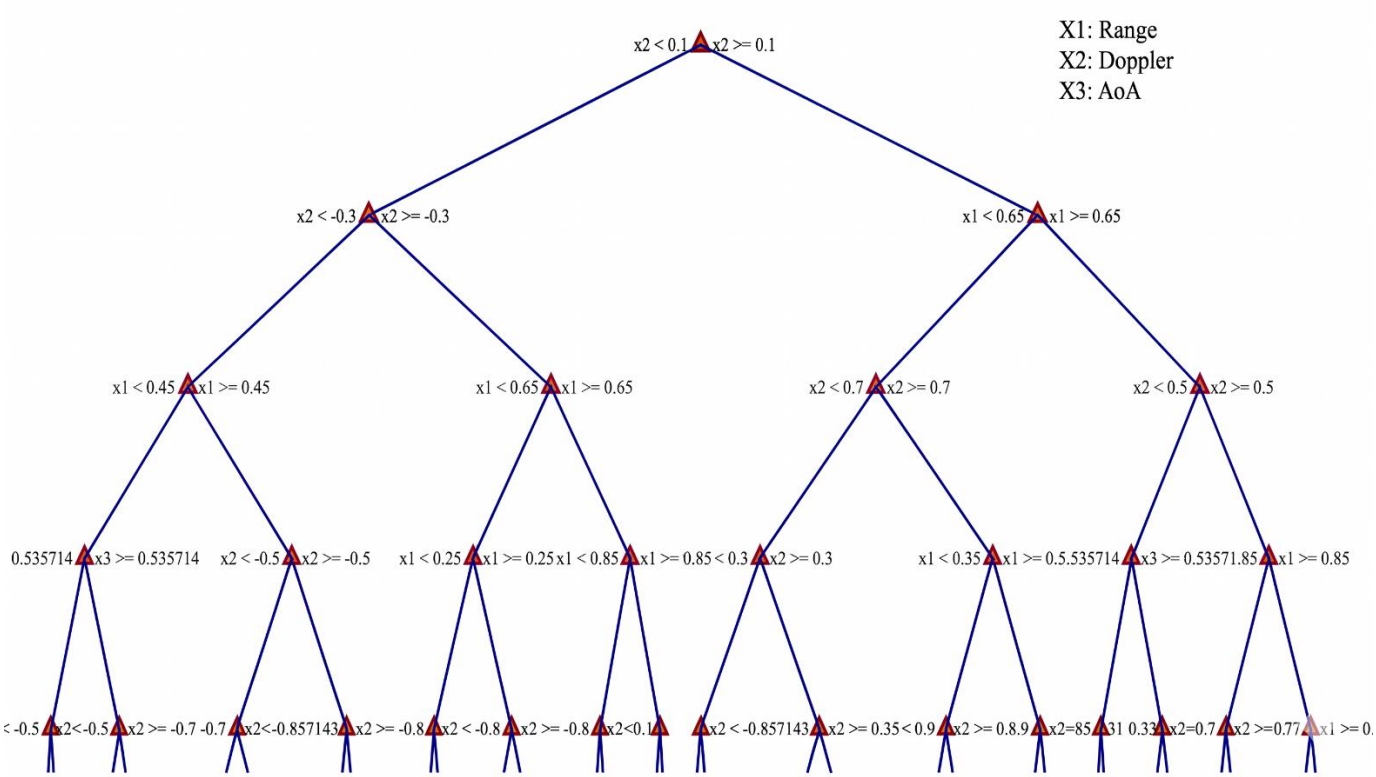

Fig. 5 Pruned Random Forest diagram

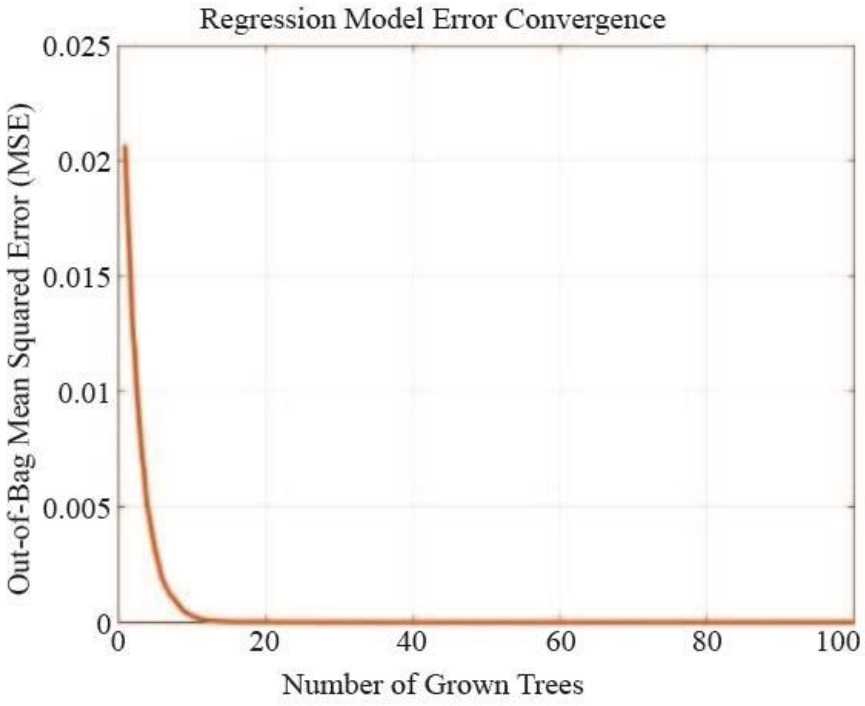

Fig. 6 Regression model convergence

Figure 6 depicts the Mean Squared Error (MSE) convergence of the regression model error covariance during training for 100 trees.

Figure 7 shows the normalized input dataset used to validate the TRF model's performance, with the TRF-predicted output indicated by a color scale (values: 0 to 1.0).

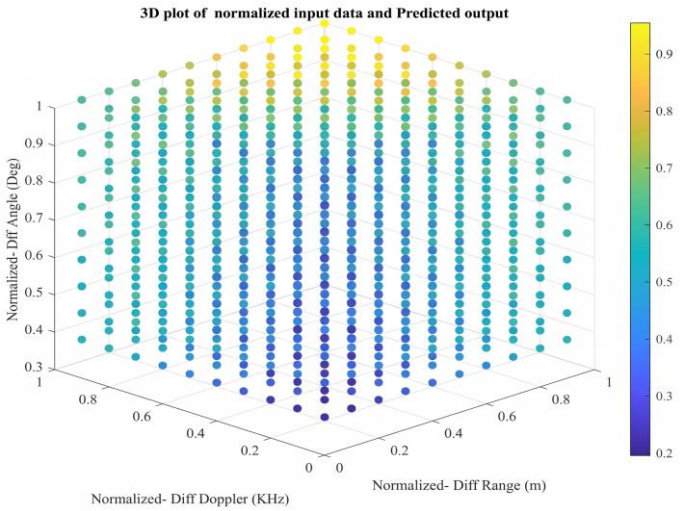

Fig. 7 Input to TRF and predicted output of TRF

Figure 8 plots the expected output, the TRF-predicted output, and the error plot. The prediction error is well within 0.03.

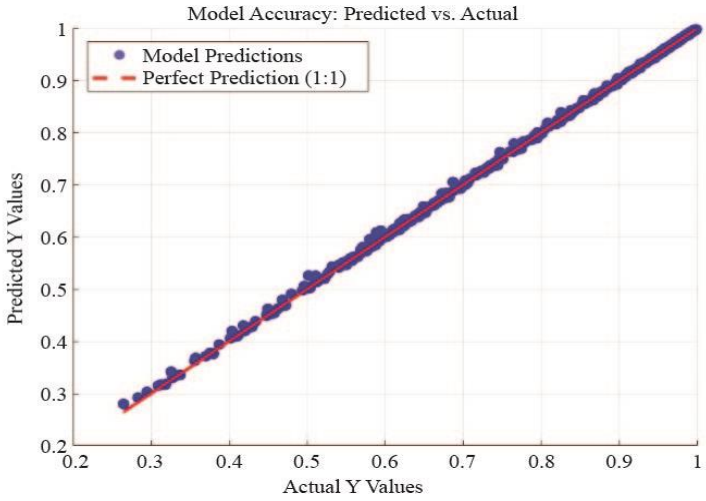

(a)

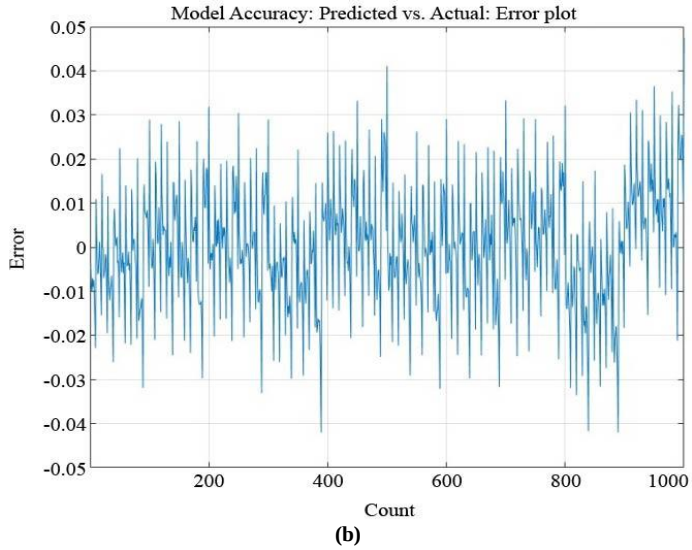

(b)

Fig. 8 RF model accuracy plot, (a) Model prediction vs actual, and (b) The error plot.

3.3. Track Classification: Spatio-Temporal Filtering

Unlike traditional static radars, this radar operates while in motion. In this context, once the radar moves past a target, that target may no longer be within its Field of View (FoV), leading to a loss of detection. Additionally, tracks that do not receive updates within a certain timeframe may become less relevant and could be removed. Some of these tracks may also be identified as false alarms. To ensure accuracy and efficiency, temporal filtering manages and refines the tracking data, helping eliminate lost, non-significant, or false alarms.

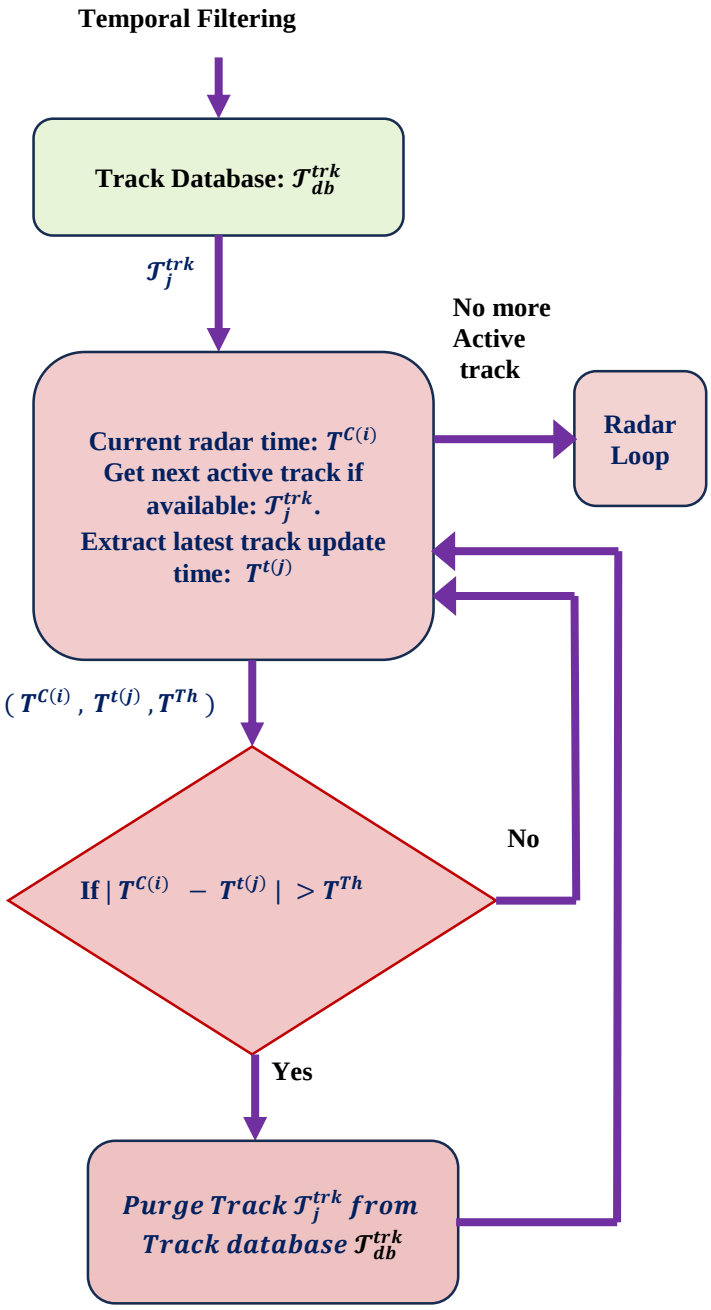

Fig. 9 Temporal filtering

Figure 9 explains the temporal filtering algorithm. The active track list is maintained along with the latest track update time. $T^{t(j)}$ for j^{th} track. Any new track update also updates the track update time. A threshold T^{Th} It is used to check the track currency. All tracks are periodically checked for currency: $T^{C(i)}$ denotes the current radar time at i^{th} instant. If any track is older than the threshold relative to the current time, it is declared lost and purged. Using this method, tracks that have moved out of FoV, have no updates, or are false alarms are periodically removed from the active track list.

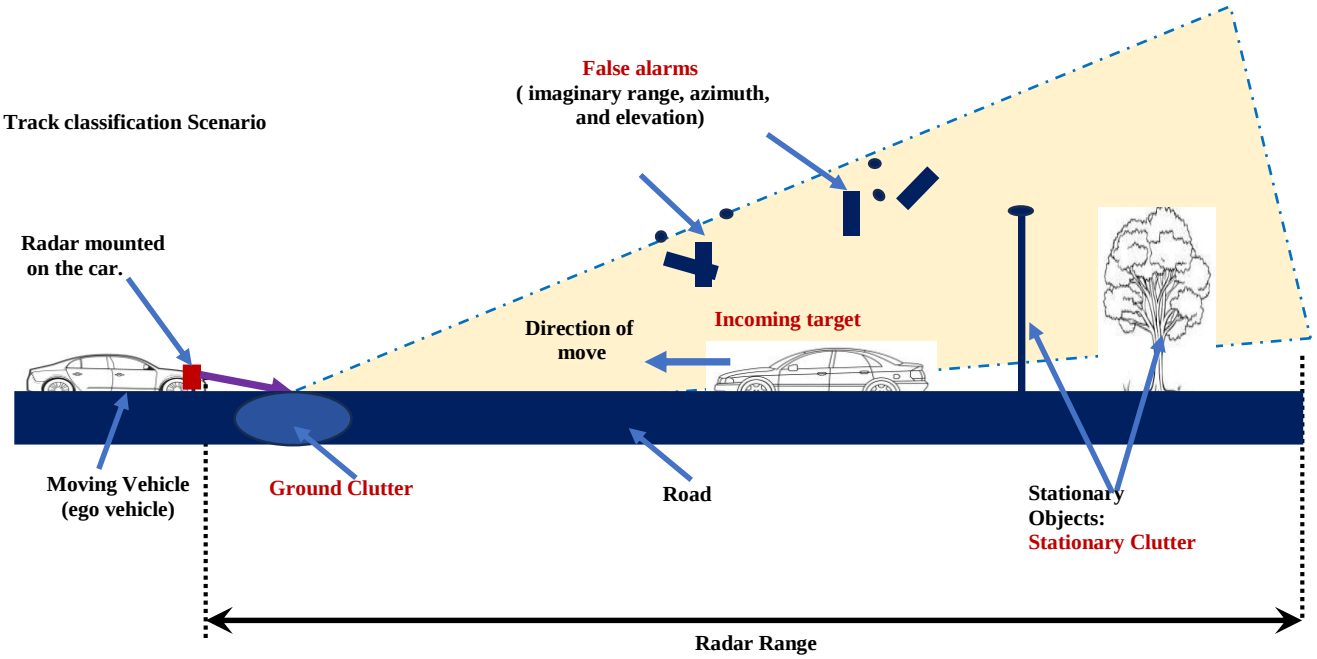

Fig. 10 Track classification scenario

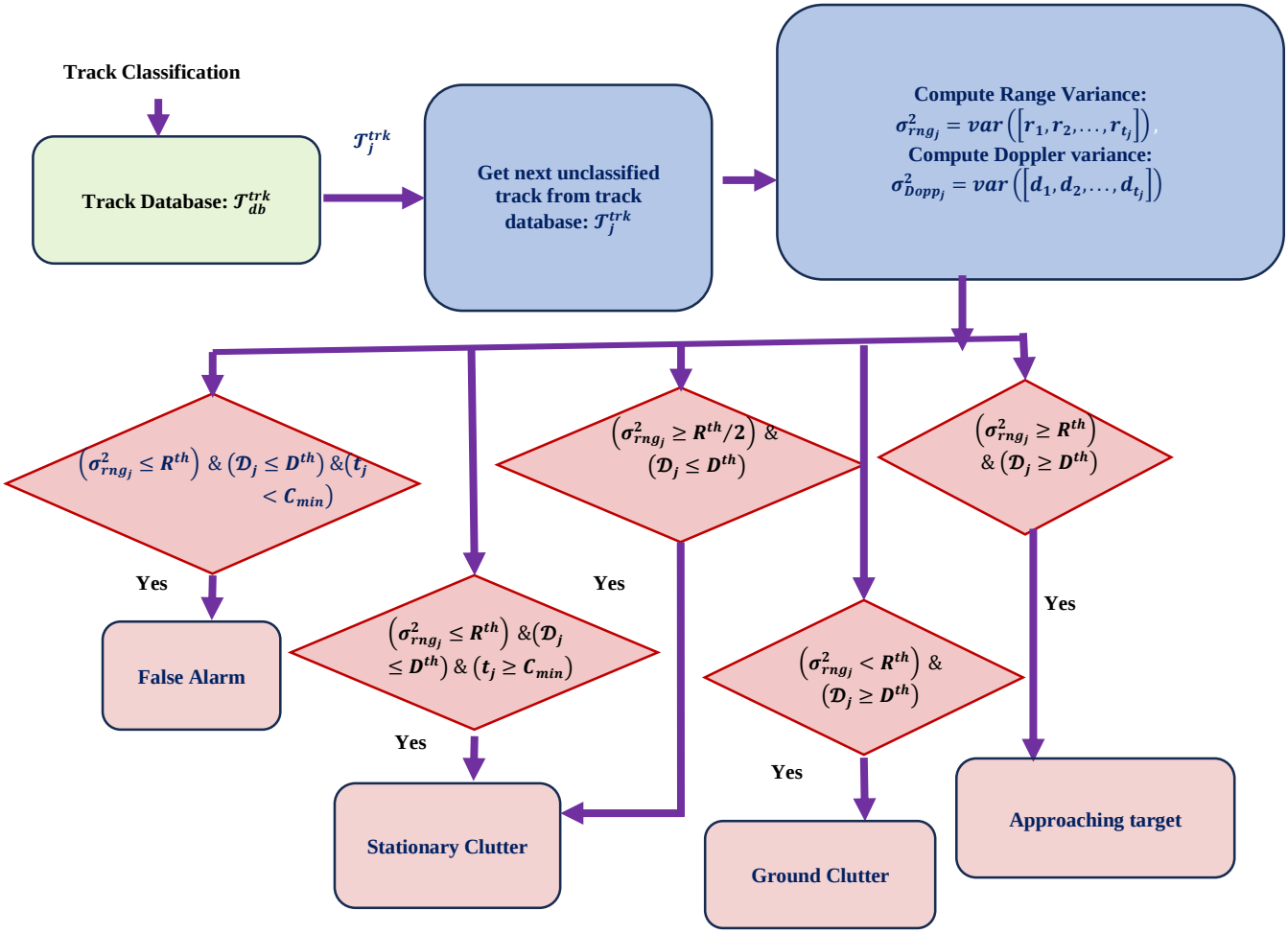

Fig. 11 Track classification algorithm

Spatial filtering classifies active tracks into four categories. The classification relies on variance measures in range and Doppler, along with the size of the track's membership. The categories and their respective classification parameters are detailed below. Figure 10 depicts the track classification scenario. The following paragraph explains this further.

- *False alarms:* A false track or false alarm persists for a few detections, exhibits low variance in both range and Doppler, and has a low track membership count.
- *Ground Clutter:* The forward-looking automotive radars are mounted at the front of the vehicle. Because of the large elevation beamwidth and low height above the ground, ground reflections are common. They have a Doppler shift equal to the vehicle speed and a shorter, near-constant range. Hence, range variance is low, but Doppler variance is high.
- *Stationary Clutter:* For a moving radar, the stationary clutter also has the same characteristics as a moving target, but the Doppler shift is due to the vehicle speed. It is characterized by high variance in both range and Doppler, and a good on-track membership count.
- *Incoming target:* The incoming target from the opposite direction has a relative speed, which is the sum of the ego vehicle speed and the approaching vehicle speed. Hence, the variance is very high in both the range and Doppler domains.

Equation (9) provides the variance calculation. Consider a track $\mathcal{T}_j^{trk}$ in the track database $\mathcal{T}_{db}^{trk}$.The ith track : $\mathcal{T}_j^{trk}$ consists of an array of associated range measurements denoted by $\mathcal{R}_j$ and the corresponding Doppler array $\mathcal{D}_j$. Let the array size be t_j. Let the threshold for the set range variance be R^{th} and similarly for Doppler, D^{th}. Let the minimum count in a track be set as C_{min}.

The range and Doppler measurements array for track $\mathcal{T}_j^{trk}$

$$\mathcal{R}_j = \left[r_1, r_2, \ldots, r_{t_j}\right]$$
$$\mathcal{D}_j = \left[d_1, d_2, \ldots, d_{t_j}\right].$$

The variance for range and Doppler measurements is

$$\sigma^2_{rng_j} = var\left(\left[r_1, r_2, \ldots, r_{t_j}\right]\right),$$
$$\sigma^2_{Dopp_j} = var\left(\left[d_1, d_2, \ldots, d_{t_j}\right]\right) \quad (9)$$

Figure 11 explains the track classification algorithm. The input is the track database. For every active track, the variance in range and Doppler is estimated. Based on the variance of the track with respect to range and Doppler, the track is classified. The following pseudocode (10) details the classification methods. A threshold is kept for both range and Doppler variance based on the experimental results. Four categories are defined for classification as explained in the following pseudocode.

1: Class False alarms:

If $\left(\sigma^2_{\mathrm{rng_j}} \le \mathrm{R^{th}}\right)$ and $\left(\mathcal{D}_\mathrm{j} \le \mathrm{D^{th}}\right)$ and$\left(\mathrm{t_j} < \mathrm{C_{min}}\right)$,

2: Class Stationary Clutter:

If $\left(\sigma^2_{\mathrm{rng_j}} \le \mathrm{R^{th}}\right)$ and $\left(\mathcal{D}_\mathrm{j} \le \mathrm{D^{th}}\right)$ and $\left(\mathrm{t_j} \ge \mathrm{C_{min}}\right)$ or

If $\left(\sigma^2_{\mathrm{rng_j}} \ge \mathrm{R^{th}}/2\right)$ and $\left(\mathcal{D}_\mathrm{j} \le \mathrm{D^{th}}\right)$,

3: Class Ground Clutter:

If $\left(\sigma^2_{\mathrm{rng_j}} < \mathrm{R^{th}}\right)$ and $\left(\mathcal{D}_\mathrm{j} \ge \mathrm{D^{th}}\right)$,

4: Class Incoming target:

If $\left(\sigma^2_{\mathrm{rng_j}} \ge \mathrm{R^{th}}\right)$ and $\left(\mathcal{D}_\mathrm{j} \ge \mathrm{D^{th}}\right)$. (10)

4. Experiments and Results

Multiple experiments were conducted covering various scenarios to validate the proposed algorithms. In all experiments, the radar was mounted on the car's bonnet, which was driven in a restricted area with different incoming and stationary targets. The following sections present the results. In all cases, the proposed RF-based technique is used for data association, KF for target tracking, and a spatiotemporal filtering technique for track classification.

4.1. Scenario #1

In this scenario, the incoming target was a car starting about 100m from the radar. Both vehicles were moving and approaching each other. Figures 12 and 13 show the ground-truth image.

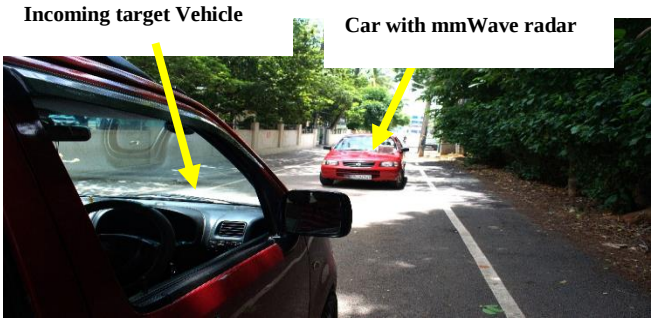

Fig. 12 A car approaching the ego vehicle

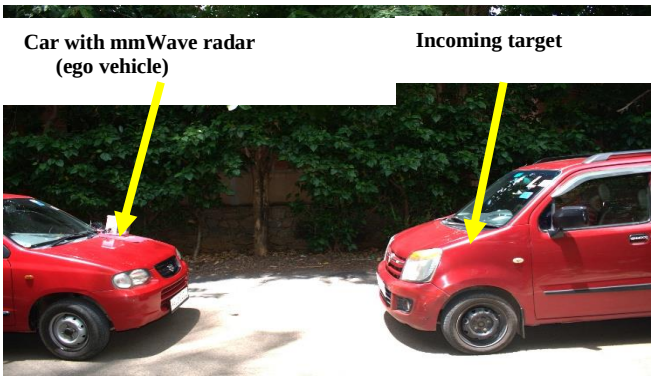

Fig. 13 Ego vehicle and approaching target vehicle

The mmWave radar tracked the incoming car from about 80m away. Figure 14 shows the Range vs. time, and Figure 15 shows the corresponding Doppler vs. Time plot. Both the range and Doppler variance of the incoming car are noticeably greater than those of stationary objects and ground clutter. This is because range and Doppler variance depend directly on the closing speed between the ego vehicle and the target. For stationary clutter, Doppler variance is comparable to that of ground clutter, as both depend only on ego-vehicle motion. However, the range variance of stationary clutter is higher because the distance between the stationary clutter and the ego vehicle decreases monotonically and depends on ego-vehicle speed.

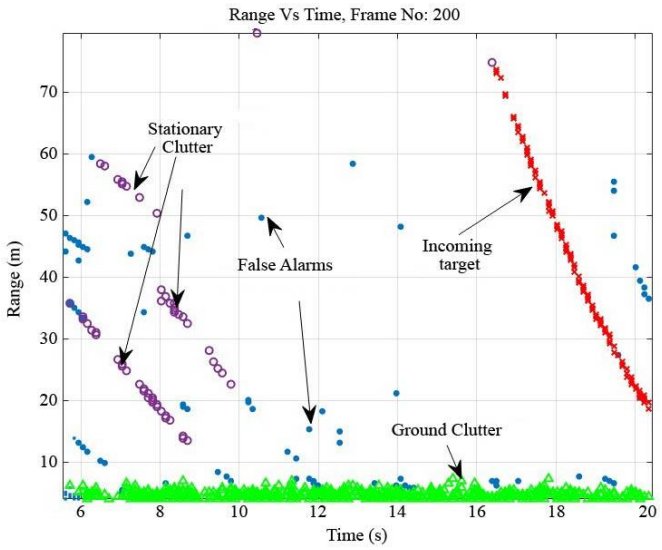

Fig. 14 Scenario#1: Range vs. time plot

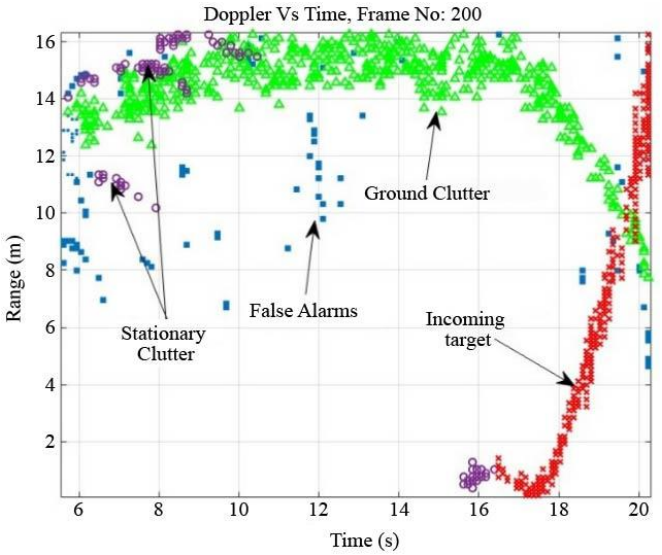

Fig. 15 Scenario#1: Doppler vs. time plot

The range variance of the ground clutter is almost constant because the radar beam hits the ground at a constant angle and from a constant height. Based on these variances, the proposed algorithm effectively classified tracks of the incoming car, stationary clutter, and ground clutter. Furthermore, false alarms are dispersed throughout, have small variances, and occur in small random groups; hence, the algorithm can recognize them as well. The figures clearly present the track classification of the four categories: incoming target, stationary clutter, ground clutter, and false alarms, with different plot types and colors.

4.2. Scenario #2

In this case, the incoming target is a person riding a two-wheeler. Figure 16 shows the ground-truth image. The corresponding tracking results are shown in Figures 17 and 18. The scenario is similar to the previous one. The incoming target Doppler envelope is higher than that of the stationary clutter and ground clutter. This results in higher variance than the other two. The target's range variation over time is also higher than the other two. Hence, the incoming two-wheeler track is easily distinguished from the stationary and ground clutter. The classification is shown in figures with different plot types and colors as used in the previous case.



Fig. 16 Scenario #2: A two-wheeler and the ego vehicle heading toward each other

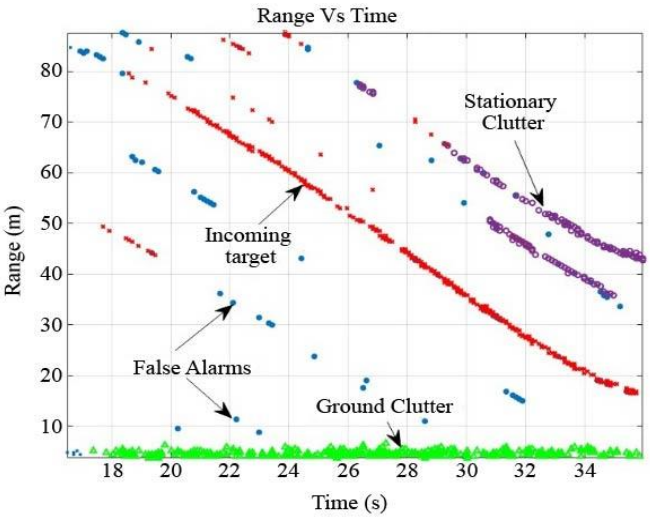

Fig. 17 Scenario#2: Range vs. time plot

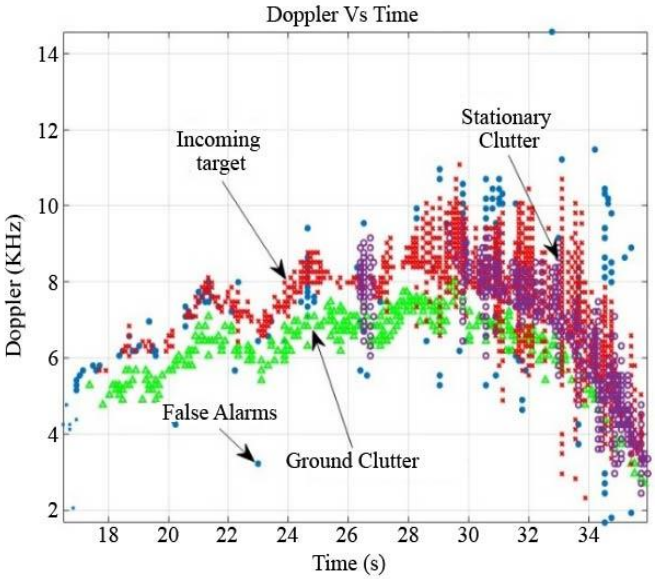

Fig. 18 Scenario#2: Doppler vs. time plot

4.3. Scenario #3

In this scenario, the experiments were conducted with an incoming car, background foliage, and a stationary pole around the target. Figure 19 shows the ground-truth image. Figures 20(a) and 20(b) show the range vs. time and Doppler vs. time plots for this scenario.

As in the previous cases, the proposed algorithm clearly classified the incoming target and the stationary clutter. Both stationary clutter and ground clutter are also visible in the plots. As in the previous cases, the same plot types and colors are used to present the results.

Occasional misclassification of stationary clutter indicates similar kinematic parameters between the incoming car and the stationary clutter, as well as occlusion of the stationary clutter by the incoming car. This is evident in Figure 20(a), where detections are missing from the stationary-clutter track.



Fig. 19 Scenario#3: Ground truth image

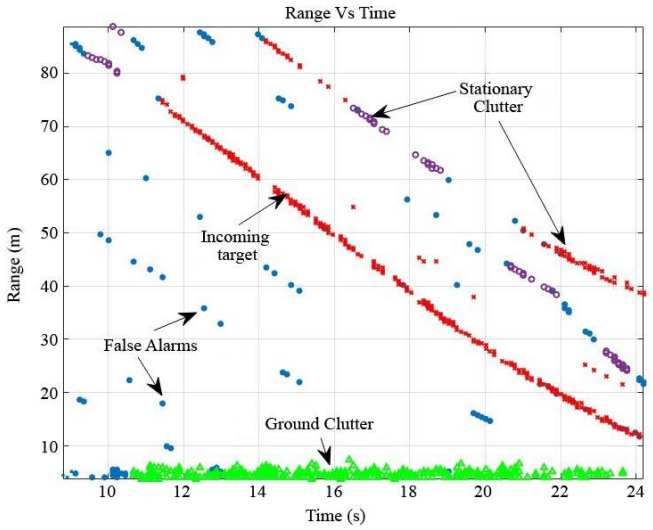

(a)

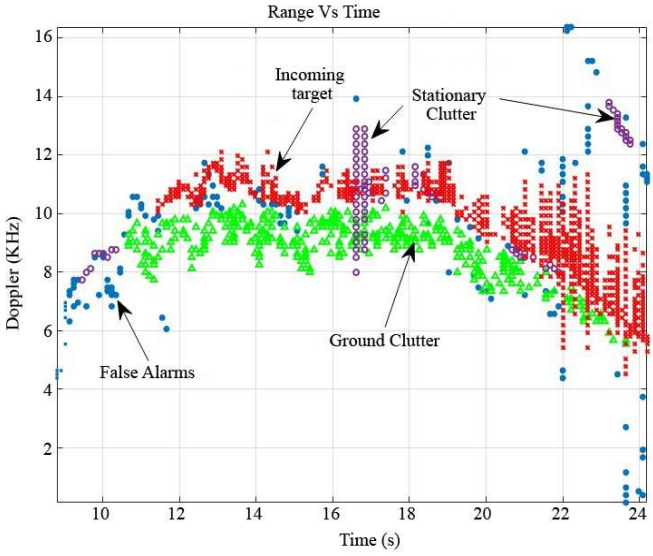

(b)

Fig. 20 Scenario #3: (a) Range vs. time plot, and (b) Doppler vs. time plot.

4.4. Classification Performance Analysis

The multi-class confusion matrix is used to compute classification accuracy. The derivation of multiclass classification is given in [29].

Table 1 shows the confusion matrix for the False alarm (Class A), Ground clutter (Class B), Stationary clutter (Class C), and Incoming car track (Class D) classes. The required data has been obtained from real-world experiments. The computation uses normalized values.

The calculation of precision and accuracy was performed as given in [29]. Precision for the different classes is as follows: False Alarm: 90%, Ground Clutter: 83.3%, Stationary Target: 89%, Incoming Target: 88.24%. The overall accuracy achieved is 93.47%.

Table 1. Confusion matrix for track classification

	Predicted				
	Class	**A**	**B**	**C**	**D**
Actuals	**A**	0.9 (PFF)	0 (PFG)	0 (PSF)	0.1 (PFT)
	B	0.0833 (PGF)	0.833 (PGG)	0.0833 (PGS)	0 (PGT)
	C	0.89 (PSF)	0 (PSG)	0.8902 (PSS)	0.0208 (PST)
	D	0 (PTF)	0 (PTG)	0.0176 (PTS)	0.8824 (PTT)

5. Conclusion

The primary objective of this research is to develop an effective solution for associating mobile radar detections and classifying tracks within ADAS. A key challenge in mobile radar is distinguishing stationary objects from approaching vehicles, which share similar kinematic characteristics. The proposed approach introduces an innovative method that addresses this concern without the need for external interfaces, such as speedometers or additional hardware. This solution has three phases. The first phase uses Random Forest-based data association to accurately match detections to their corresponding clusters. The second phase applies a Kalman filter for tracking. The third phase classifies the target track into one of four categories using spatiotemporal filtering techniques. Additionally, this research includes algorithm validation, which underwent thorough testing using data collected from real-world driving situations. The findings indicate a commendable classification accuracy of approximately 93%, reflecting the proposed approach's potential effectiveness. Further work is needed to improve track classification performance because the current method occasionally misclassifies tracks with very similar kinematic parameters or due to track drops caused by occlusion or other factors.

Conflicts of Interest

The authors declare no conflict of interest regarding the publication of this paper.

Funding Statement

The authors declare that no funding supported this research.

Acknowledgement

The authors sincerely thank the Defense Institute of Technology, Pune, for their valuable study materials and guidance.

Author's contribution

Author 1: Conceptualization, problem analysis, algorithm/methodology development, experiment conduct and data collection, algorithm validation, and preparing the original draft report.

Author 2: Critical review of the algorithm, supervision, and final review and editing.

Author 3: Critical review of radar parameters, supervision, and final review and editing.

References

[1] Marco Galvani, "History and Future of Driver Assistance," *IEEE Instrumentation & Measurement Magazine*, vol. 22, no. 1, pp. 11-16, 2019. [CrossRef] [Google Scholar] [Publisher Link]

[2] Shunqiao Sun, Athina P. Petropulu, and H. Vincent Poor, "MIMO Radar for Advanced Driver-Assistance Systems and Autonomous Driving: Advantages and Challenges," *IEEE Signal Processing Magazine*, vol. 37, no. 4, pp. 98-117, 2020. [CrossRef] [Google Scholar] [Publisher Link]

[3] Christian Waldschmidt, Juergen Hasch, and Wolfgang Menzel, "Automotive Radar—from First Efforts to Future Systems," *IEEE Journal of Microwaves*, vol. 1, no. 1, pp. 135-148, 2021. [CrossRef] [Google Scholar] [Publisher Link]

[4] Florian Engels et al., "Automotive Radar Signal Processing: Research Directions and Practical Challenges," *IEEE Journal of Selected Topics in Signal Processing*, vol. 15, no. 4, pp. 865-878, 2021. [CrossRef] [Google Scholar] [Publisher Link]

[5] Xinrong Li et al., "Signal Processing for TDM MIMO FMCW Millimeter-Wave Radar Sensors," *IEEE Access*, vol. 9, pp. 167959-167971, 2021. [CrossRef] [Google Scholar] [Publisher Link]

[6] Sandeep Rao, Rajan Narasimha, and Shunqiao Sun, "Signal Processing Challenges in Automotive Radar," *ICASSP 2025 - 2025 IEEE International Conference on Acoustics, Speech and Signal Processing (ICASSP)*, Hyderabad, India, pp. 1-5, 2025. [CrossRef] [Google Scholar] [Publisher Link]

[7] T. Fortmann, Y. Bar-Shalom, and M. Scheffe, "Sonar Tracking of Multiple Targets Using Joint Probabilistic Data Association," *IEEE Journal of Oceanic Engineering*, vol. 8, no. 3, pp. 173-184, 1983. [CrossRef] [Google Scholar] [Publisher Link]

[8] Shuang Liang et al., "Cauchy-Schwarz Divergence-Based Set Joint Probabilistic Data Association Filter for Tracking Multiple Objects in Cluttered Environment," *IEEE Transactions on Geoscience and Remote Sensing*, vol. 62, pp. 1-15, 2024. [CrossRef] [Google Scholar] [Publisher Link]

[9] Jie Ren, Lingling Zhang, and Jiaao Liu, "Research and Implementation of 77GHz Automotive Radar Target Detection Technology," *2023 6th International Conference on Information Communication and Signal Processing (ICICSP)*, Xi'an, China, pp. 517-521, 2023. [CrossRef] [Google Scholar] [Publisher Link]

[10] Konstantinos Fatseas, Marco J.G. Bekooij, and Willem P. Sanberg, "Optimizing PointNet++ and DBSCAN for Object Detection in Automotive Radar Point Clouds," *2024 21st European Radar Conference (EuRAD)*, Paris, France, pp. 39-42, 2024. [CrossRef] [Google Scholar] [Publisher Link]

[11] Mark A. Southcott, and Chen Liu, "Poster: Improved DBSCAN using Modified Epsilon for Static Scene Clustering," *2025 IEEE 3rd International Conference on Mobility, Operations, Services and Technologies (MOST)*, Newark, DE, USA, pp. 1-3, 2025. [CrossRef] [Google Scholar] [Publisher Link]

[12] Mark A. Southcott, and Chen Liu, "TDM: A Novel Density-Based Clustering Algorithm for Automotive Radar Applications," *2026 IEEE 4th International Conference on Mobility, Operations, Services and Technologies (MOST)*, Detroit, MI, USA, pp. 26-34, 2026. [CrossRef] [Google Scholar] [Publisher Link]

[13] Bao Ming Ding et al., "Enhanced Multiple DBSCAN Algorithm for Traffic Detection using mmWave Radar," *2023 IEEE International Conference on Mobility, Operations, Services and Technologies (MOST)*, Detroit, MI, USA, pp. 105-111, 2023. [CrossRef] [Google Scholar] [Publisher Link]

[14] Hanchen Li et al., "Multi-Dimensional DBSCAN Clustering Approach for Millimeter Wave Radar Point Cloud Data," *2024 International Conference on Microwave and Millimeter Wave Technology (ICMMT)*, Bejing, China, vol. 1, pp. 1-3, 2024. [CrossRef] [Google Scholar] [Publisher Link]

[15] Tim Dieter Eberhardt et al., "What the Cluster: An Unsupervised Framework to Segment Automotive Doppler Radar Point Clouds," *2024 IEEE International Conference on Vehicular Electronics and Safety (ICVES)*, Ahmedabad, India, pp. 1-6, 2024. [CrossRef] [Google Scholar] [Publisher Link]

[16] Lulu Liu et al., "Clutter Detection in Automotive Radar Point Clouds based on Deep Learning with Self-Attention," *2023 8th International Conference on Signal and Image Processing (ICSIP)*, Wuxi, China, pp. 424-428, 2023. [CrossRef] [Google Scholar] [Publisher Link]

[17] Md. Monjur Ul Hasan et al., "Piecemeal Clustering: A Self-Driven Data Clustering Algorithm," *IEEE Access*, vol. 10, pp. 129985-130000, 2022. [CrossRef] [Google Scholar] [Publisher Link]

[18] Xirui Xue et al., "Resolvable Cluster Target Tracking based on the DBSCAN Clustering Algorithm and Labeled RFS," *IEEE Access*, vol. 9, pp. 43364-43377, 2021. [CrossRef] [Google Scholar] [Publisher Link]

[19] Sihem Jebari, Abir Smiti, and Aymen Louati, "AF-DBSCAN: An Unsupervised Automatic Fuzzy Clustering Method Based on DBSCAN Approach," *2019 IEEE International Work Conference on Bioinspired Intelligence (IWOBI)*, Budapest, Hungary, pp. 1-6, 2019. [CrossRef] [Google Scholar] [Publisher Link]

[20] Chengcheng Xu et al., "Spatial Data Association Target Fusion of Multi-Sensor for Vehicle Detection," *2024 8th CAA International Conference on Vehicular Control and Intelligence (CVCI)*, Chongqing, China, pp. 1-6, 2024. [CrossRef] [Google Scholar] [Publisher Link]

[21] Huiping Su et al., "Object Detection in Adverse Weather for Autonomous Vehicles based on Sensor Fusion and Incremental Learning," *IEEE Transactions on Instrumentation and Measurement*, vol. 73, pp. 1-10, 2024. [CrossRef] [Google Scholar] [Publisher Link]

[22] Arindam Sengupta, Lei Cheng, and Siyang Cao, "Robust Multiobject Tracking using mmWave Radar-Camera Sensor Fusion," *IEEE Sensors Letters*, vol. 6, no. 10, pp. 1-4, 2022. [CrossRef] [Google Scholar] [Publisher Link]

[23] Adam A. Khabachirov et al., "Multiple Objects Tracking Algorithm for Car Radar," *2025 7th International Youth Conference on Radio Electronics, Electrical and Power Engineering (REEPE)*, Moscow, pp. 1-6, 2025. [CrossRef] [Google Scholar] [Publisher Link]

[24] Mahdi Koloushani et al., "Multi-Target Tracking in the Presence of Velocity Ambiguity for Automotive Radar," *ICASSP 2024 - 2024 IEEE International Conference on Acoustics, Speech and Signal Processing (ICASSP)*, Seoul, Korea, pp. 8851-8855, 2024. [CrossRef] [Google Scholar] [Publisher Link]

[25] László Lindenmaier et al., "Comparison of Track Management Strategies in Automotive Track-to-Track Fusion Algorithms," *2025 IEEE 23rd World Symposium on Applied Machine Intelligence and Informatics (SAMI)*, Stará Lesná, Slovakia, pp. 377-384, 2025. [CrossRef] [Google Scholar] [Publisher Link]

[26] G.S. Vandana, Bethi Pardhasaradhi, and Pathipati Srihari, "Intruder Detection and Tracking using 77 GHz FMCW Radar and Camera Data," *2022 IEEE International Conference on Electronics, Computing and Communication Technologies (CONECCT)*, Bangalore, India, pp. 1-6, 2022. [CrossRef] [Google Scholar] [Publisher Link]

[27] Shashank SK et al., "Enhanced Intruder Detection using mmWave Radar: A Spatiotemporal Clustering Approach for Robust Human Detection," *2024 IEEE 21st India Council International Conference (INDICON)*, Kharagpur, India, pp. 1-6, 2024. [CrossRef] [Google Scholar] [Publisher Link]

[28] Ramon Nitzberg, "Constant-False-Alarm-Rate Signal Processors for Several Types of Interference," *IEEE Transactions on Aerospace and Electronic Systems*, vol. 8, no. 1, pp. 27-34, 1972. [CrossRef] [Google Scholar] [Publisher Link]

[29] Johan Erbani et al., "Confusion Matrices: A Unified Theory," *IEEE Access*, vol. 12, pp. 181372-181419, 2024. [CrossRef] [Google Scholar] [Publisher Link]